High loading of single atomic iron sites in Pyrolysed Fe–NC oxygen reduction catalysts for proton exchange membrane fuel cells

Asad Mehmood, Mengjun Gong, Frédéric Jaouen, Aaron Roy, Andrea Zitolo, Anastassiya Khan, Moulay-Tahar Sougrati, Mathias Primbs, Alex Martinez Bonastre, Dash Fongalland, et al.

High Loading of Single Atomic Iron Sites in Pyrolysed Fe-NC Oxygen Reduction Catalysts for Proton Exchange Membrane Fuel Cells

Asad Mehmood[1], Mengjun Gong[1], Frédéric Jaouen[2], Aaron Roy[2], Andrea Zitolo[3], Anastassiya Khan[3], Moulay-Tahar Sougrati[2], Mathias Primbs[4], Alex Martinez Bonastre[5], Dash Fongalland[5], Goran Drazic[6], Peter Strasser[4], Anthony Kucernak[1]*

[1]Department of Chemistry, Molecular Sciences Research Hub, Imperial College London, White City Campus W12 0BZ London, United Kingdom.

[2]ICGM, Univ. Montpellier, CNRS, ENSCM, Montpellier, France. [3]Synchrotron SOLEIL, L'orme des Merisiers, BP 48, Saint Aubin, 91192 Gif-sur-Yvette, France.

[4]Department of Chemistry, Chemical Engineering Division, Technical University of Berlin, 10623 Berlin, Germany.

[5]Johnson Matthey Technology Center, Blount's Court, Sonning Common, Reading RG4 9NH, United Kingdom.

[6]Department of Materials Chemistry, National Institute of Chemistry, Hajdrihova 19, SI-1000 Ljubljana, Slovenia.

*Correspondence to: Anthony Kucernak. Email: anthony@imperial.ac.uk

Abstract: Fe-NCs require high active site density (SD) to meet the performance targets as cathode catalysts in proton exchange membrane fuel cells (PEMFCs). SD is generally limited to a maximum of 1-3 wt%(Fe). Attempts to achieve higher contents of atomic iron have hitherto led to the undesired formation of iron-containing nanoparticles. By not including iron in the initial synthesis step we achieve 7 wt% iron coordinated solely as single atom Fe-N_4 sites identified by ^{57}Fe cryo Mössbauer spectroscopy and X-ray absorption spectroscopy. SD values obtained by *in situ* nitrite stripping and *ex situ* CO chemisorption methods are 4.7x10^{19} and 7.8x10^{19} sites·g^{-1}, with a turnover frequency of 5.4 electrons·sites^{-1}·s^{-1} at 0.80 V in H_2SO_4 electrolyte. The catalyst delivers excellent PEMFC performance with current densities of 41 mA·cm^{-2} at 0.90 $V_{iR\text{-}free}$ using H_2-O_2 (10.6 A·g^{-1}) and 145·mA cm^{-2} at 0.80 V (199 mA·cm^{-2} at 0.80 $V_{iR\text{-}free}$) using H_2-air.

Main: Proton exchange membrane fuel cells (PEMFCs) as zero-emission power generation system are an appealing option for a variety of applications, particularly for the electrification of transportation sector from small/medium size cars to heavy duty vehicles.[1,2] Mass production and commercialisation of fuel cells is, however, significantly dependent on their cost competitiveness. Currently, the inevitable use of Pt-based catalysts contributes about 41% to the total stack costs.[3] The sluggish kinetics of oxygen reduction reaction (ORR) require around 80% of total Pt loadings at the PEMFC cathode. The development of platinum-group metal-free (PGM-free) catalysts for ORR to replace Pt has been pursued actively for over a decade now and promising activity levels were reported for the class of M-NC catalysts where M is a transition metal, with Fe and Co leading to the highest ORR activity.[4-6] The metal ions, e.g. Fe, are stabilised by nitrogen ligands of nitrogen-doped carbon matrix (NC) to form Fe-N_x coordination, strongly resembling the metal-N_4 core in metal porphyrins and phthalocyanines.[4,7-10] The first ever report on the ORR activity of M-NCs dates back to the early 1960s when Jasinski found that metal phthalocyanines catalyse the oxygen reduction in alkaline electrolyte [11,12] and the activity in acidic electrolyte was later improved by others using a high temperature pyrolysis.[13]

In recent years, tremendous progress has been made in improving the acidic ORR activity of M-NC materials particularly with Fe-NCs. However, their activity and stability levels are still well short of performance criteria [2,5,14] defined for displacing PGM catalysts at the cathode, highlighting the importance of further activity upgradation. In order to enhance the ORR activity, many different synthesis strategies have been pursued for tuning the Fe-NC structures.[7,8,15-20] The main goal is to maximise the abundance of atomically dispersed iron as Fe-N_x and increase their intrinsic activity. However, only limited success has been seen so far, with most of the reported Fe-NCs reaching atomic iron content of between 0.5 – 2.0 wt%, higher Fe content leads to partial

or complete Fe clustering as metallic nanoparticles, iron carbide and iron nitride etc. during pyrolysis.[9,21] Recently, a few new strategies have been introduced to improve atomic Fe dispersion, among which silica coating of Fe-coordinated C, N precursor(s) is most notable for suppressing the aggregation of iron atoms during high-temperature pyrolysis, however the amount of atomically dispersed iron can only be improved to 3 wt%.[22-25] Moreover, the added synthetic complexity for incorporation of silica or other such coating strategies becomes an important point of concern in the context of their feasibility for scaling up.[26] In fact, the bottleneck of low Fe site density in state-of-the-art Fe-NCs stems from the direct pyrolysis strategy. Iron with its relatively more noble character has higher tendency to undergo carbo-thermal reduction to form metallic particles as compared to some other metals, e.g. Zn or Mg, which can form similar M-N_x sites and are more stable in their oxidised state (M^{2+}).[27-29] Therefore, decoupling the formation step of Fe-N_4 sites from the high temperature pyrolysis seems critical for overcoming this dilemma. This was successfully demonstrated by Mehmood et al. in a proof-of-concept study where thermally stable Mg-N_4 sites imprinted in a porous Mg-NC matrix which was then converted to Fe-N_4 moieties via low temperature metalation/transmetalation with iron.[30] The final Fe-NC catalyst consisted exclusively of atomic Fe sites with up to 1.30 wt% iron. Later on, Menga et al. showed that Zn-N_4 sites could also be used to prepare Fe-NCs under this active-site imprinting concept.[31] A high-temperature transmetalation concept utilising chemical vapor deposition of iron single atoms into NC matrix has been recently demonstrated by Jia's group.[32,33]

In this work, we report significant progress in increased Fe-N_x site density by combining the advantages of post-pyrolysis formation of Fe-N_4 moieties and high density of atomically coordinated Zn sites in zeolitic imidazolate framework (ZIF) materials. The resultant Fe-NC

catalyst consists of. 7 wt% Fe-N_4 sites, identified by ^{57}Fe Mössbauer spectroscopic measurements performed at 5 K, inductively coupled plasma mass spectrometry (ICP-MS), and X-ray absorption spectroscopy (XAS). Cryo Mössbauer measurements also provide critical insights into the structural evolution of Fe-N_4 sites before and after activation. *In situ* nitrite stripping and *ex situ* CO chemisorption techniques are utilised for quantification of the site densities (SDs) and turnover frequencies (TOFs).[34,35] In the optimised Fe-NC catalyst, SD values of 4.67 x 10^{19} sites g^{-1} (4.04 x 10^{16} sites m^{-2}) and 7.8 x 10^{19} sites g^{-1} (6.8 x 10^{16} sites m^{-2}) are obtained with nitrite stripping[34,36] and CO chemisorption[35,37] methods, respectively, which are far greater than the four benchmark Fe-NCs (3 – 18x greater electrochemically accessible SD values based on *in situ* nitrite stripping method).[38] Such high density of Fe-N_4 sites translates into excellent ORR activity in rotating ring disk electrode (RRDE) as well as in fuel cell measurements. In PEMFC tests under H_2-O_2 environment, we show that the optimised Fe-NC catalyst performs impressively with an excellent current density of 41.3 mA cm^{-2} at the reference cell voltage of 0.90 $V_{iR\text{-}free}$ (mass activity of 10.59 A g^{-1}) higher than the reported values that are in 25 – 35 mA cm^{-2} range and achieved using higher Fe-NC loadings (5-6 mg cm^{-2}), corresponding to mass activities between 4 – 6 A g^{-1}.[26,33,39,40]

Results

Analysis of SD and TOF requirements for achieving activity targets:

If the iron in an Fe-NC catalyst is randomly distributed through the material in atomic sites then not all of that iron will be present on the surface, i.e. some will be “buried” and inaccessible. Consequently, with a random distribution, the amount of iron accessible on the catalyst will scale with the surface area of the catalyst. Fig. 1a shows the number of iron sites increases in a near linear fashion with catalyst specific surface area up until all the iron is on the surface which

occurs in the range a specific surface area of ca. 1244-1316 $m^2\ g^{-1}$ (7 wt%(Fe) → 0 wt%(Fe) see supplementary note S1 and Figs. S1-S5 for calculation details and additional discussion associated with the proportion of edge/basal plane sites and Table S1 for estimates of basal, edge and buried Fe sites in our catalyst). Note this surface area is not the maximum possible surface area of the catalyst which is twice the associated value and reflects the fact that once the catalyst is composed of two graphene-like sheets, all iron must be on the surface. If there is segregation of iron to or away from the surface, then the corresponding curves in Fig.1a will either bow above (segregation to the surface) or below (segregation to the bulk) those lines but will still have the same endpoints. As the mass loading of iron increases from 1 to 7 wt%, the curves increase concomitantly, and the average separation between surface iron atoms on the surface, (r_{Fe-Fe}^{avg} , independent of catalyst surface area) decreases from 3.1 to 1.1 nm. As most Fe-NC catalysts have a specific surface area of around 600-800 $m^2\ g^{-1}$, it is expected that only about half of total iron is exposed on the surface. Even with a high iron content (7 wt% - i.e. 1.6 at%) and high specific surface area catalyst (e.g. 1000 $m^2\ g^{-1}$), one can achieve a maximum of only around 7.5×10^{20} sites g^{-1}. This imposes a realistic upper limit of site density on these sorts of catalysts as even achieving a metal loading of 7 wt% with atomic dispersion, as we have achieved in this study, is difficult.

A further requirement which needs to be achieved in these catalysts is having an appropriate TOF for the ORR. The mass specific current density (j_m) can be expressed as the product of the turnover frequency and surface site density:

$$j_m[A\ g^{-1}] = SD[sites\ g^{-1}] \times TOF[electrons\ site^{-1}s^{-1}] \times e[C\ electron^{-1}] \qquad \text{Equation 1}$$

The US department of energy (DOE) and the fuel cells and hydrogen joint undertaking (FCH JU) specify expected requirements for the performance of catalysts at 0.90 V under appropriate conditions, and these numbers are usually expressed in terms of a geometric current densities, which can be obtained by multiplying j_m by the area specific catalyst loading under the assumption that mass transport effects are insignificant. In Fig. 1b, we use the DOE requirement for 0.044 A cm^{-2} to assess the required SD and TOF for Fe-NC catalysts as a function of electrode loading (solid lines). Note that as catalyst loading increases, the requirements for SD and TOF decrease, but this is at the expense of very thick catalyst layers (25 μm → 250 μm as loading increases from 1 → 10 mg cm^{-2}) associated with low density of these catalysts (~0.4 g cm^{-3}). Very thick catalyst layers pose problems at high current densities due to mass transport effects, and although high loadings might allow achievement of an areal current density target at high potentials, they are not helpful in making a fuel cell operate in the high current regime, and may lead to optimisation strategies which are inappropriate for practical devices. Also displayed in Fig.1b are the equivalent performance of Pt/C catalysts towards the same DOE target (green dots, and dotted line), for which the required DOE requirements are an activity of 0.44 mA mg_{Pt}^{-1} at a loading of 0.1 mg_{Pt} cm^{-2} at 0.90 V – i.e. the same geometric current density of 0.044 A cm^{-2}. As one can estimate the "site density" on these platinum nanoparticles as equal to the number of platinum atoms on the particle surface (i.e. one Pt surface atom = 1 site), this also allows us to specify the required TOF for the ORR on these catalysts as a function of platinum specific surface area (i.e. electrochemical surface area). Typical fuel cell catalysts have platinum surface areas of 90 - 100 m^2 g^{-1}. In this case, this would correspond to a TOF of about 2 electrons Pt_{surf}^{-1} s^{-1}. At a platinum loading on carbon of ca. 40 wt%, the catalyst layer thickness is then about 6 μm – significantly thinner than the Fe-NC catalyst layers. If we were able to achieve the

same TOF on the Fe-NC catalysts as that of Pt, this would represent an outstanding achievement as Pt performance is several orders of magnitude higher than current performance levels. Thus, we set this TOF as the upper limit for Fe-NC catalysts. Furthermore, geometric arguments of the type discussed above and realised in Fig. 1a suggest that achieving an Fe-NC active site density higher than ~10^{21} sites g^{-1} is not realistically possible. Thus, to achieve the required performance, we need to produce catalysts with SDs and TOFs within the green region, and preferably in the upper righthand corner of that zone. However, there is a difficulty in achieving the high surface SD required by Fig. 1b, as these can only be achieved with high metal loadings and as described above Fe-NCs are typically limited to maximum iron content of 3 wt%. Agglomeration of atomic sites to nanoparticles for higher iron contents drastically decreases the number of metal atoms available for reaction sites.[22-25] In order to overcome this barrier, we have developed a modified catalyst synthesis, which allows high quantities of iron whilst avoiding the production of nanoparticles, improving the number of single atom sites beyond the state-of-art. The SD (measured by nitrite stripping) and TOF (calculated from H_2-O_2 PEMFC current density at 0.90 $V_{iR\text{-}free}$) values achieved in this study are represented by a star in Fig. 1b which falls in the "zone of opportunity" triangle.

Fig. 1c sequentially presents the catalyst synthesis steps. In the first step, a Zn-NC matrix rich with Zn-N_x sites is prepared by pyrolysing a Zn-based metal organic framework (MOF), namely a commercial ZIF-8 (Basolite® Z1200). The pyrolysis is performed at 900 °C to maximise the Zn content (~ 25 wt% as measured by ICP-MS) in the resulting Zn-NC. The rationale behind this strategy was to generate a nitrogen doped carbon scaffold containing a high concentration of Zn-N_x sites, which are then converted to □-N_x sites (empty square = metal vacancy/protonated site) after Zn leaching, which could then be exploited to generate a high concentration of Fe-N_x sites

in a subsequent step(s). Fe coordination is carried out by first stripping out Zn from the surface-accessible Zn-N_x sites in the Zn-NC by acid leaching, thus creating plenty of vacant □-N_x moieties (Zn leached matrix is denoted as □-NC in Fig. 1c), where Fe^{2+} ions could easily bind when refluxing in iron(II) chloride solution to form Fe-N_4 sites (metalation). In parallel, some Fe-N_4 sites could also be formed via transmetalation where Fe ions exchanged with any of the accessible unleached (acid-stable) Zn-N_x sites in □-NC matrix. The Fe-NC catalyst thus produced contained high Fe content of 7 wt%. Here, a notable point is that while ZIF-8 has been used as a precursor for preparing Fe-NCs, an Fe-N_4 bulk site density corresponding to 7 wt% range has never been hitherto achieved. This indicates that the conventional synthesis techniques based on excessive evaporation of Zn and associated nitrogen sites at temperatures ≥ 1000 ^{o}C, could not effectively utilise the full potential of ZIF-8 as a precursor material. As shown in Fig. 1c, the unactivated catalyst, denoted as Fe-NC^{U}, is finally subjected to a high temperature activation step in the presence of dicyandiamide (DCDA, a "blowing" agent) to yield Fe-$NC^{\Delta-DCDA}$, where "Δ" represents activation and "DCDA" the presence of dicyandiamide. A control sample denoted as Fe-NC^{Δ} was prepared and activated identically, except that no DCDA was added in the activation step.

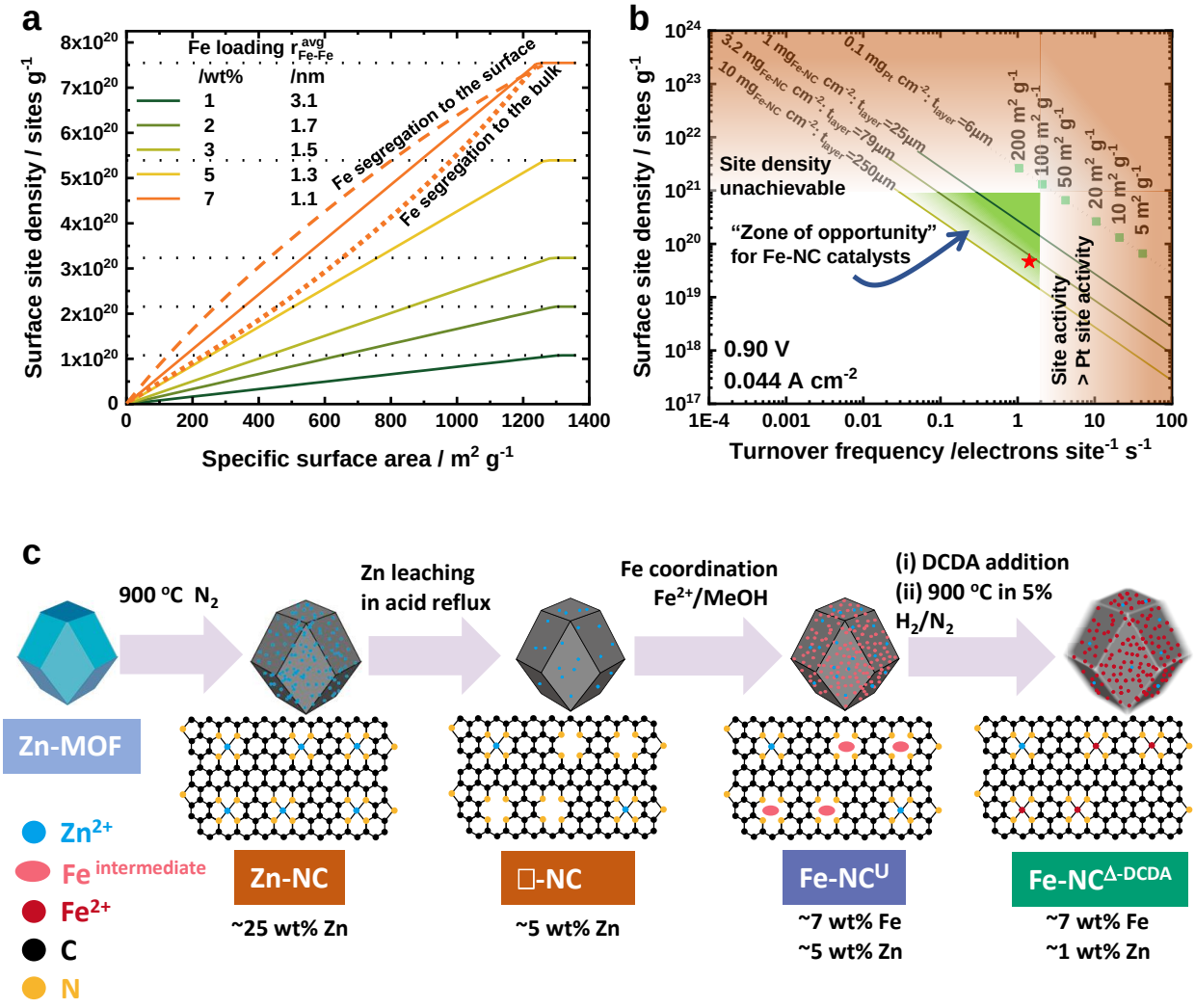

Fig. 1. Calculation of Fe-NC site density and effect on performance. (a) Calculated surface site density (calculation details in supplementary note S1) as a function of different iron contents and catalyst specific surface area for single atom dispersed catalysts. Average iron-iron separation is constant for each iron loading and at high specific surface area (~1200 m^2g^{-1}), all iron is on the surface (horizontal dotted line); (b) surface site density versus turnover frequency plot showing Fe-NC catalyst requirements to achieve area specific current density of 0.044 A cm^{-2} at 0.90 V as a function of catalyst loading (solid lines). The star represents the SD and TOF values achieved with Fe-NC catalyst in this study. Comparison to Pt/C catalyst performance requirements for the same current density at a Pt loading of 0.1 mg cm^{-2} using the calculated surface site density of Pt nanocrystals, (dots- specific catalyst surface area, dotted line); (c) cartoon illustrating the synthetic approach for high Fe loading Fe-NC catalyst. A Zn-MOF is pyrolysed at 900 °C in the first step to obtain a Zn-NC matrix with abundant Zn-N_x sites followed by Zn leaching (leached matrix is labelled as □-NC) and then Fe coordination to obtain the unactivated Fe-NC^U catalyst. In the final step, Fe-NC^U is activated at 900 °C in the presence of DCDA activating agent.

Structural characterisation of Fe-NC catalyst:

The synthesised Fe-NC catalysts were analysed for their physicochemical features (Fig. 2). Transmission electron microscopy (TEM) images (Figs. 2a and S6) show truncated polyhedron morphology for the Fe-NC^{U} catalyst, identical to the unpyrolysed ZIF-8 particles. The majority of the primary catalyst particles are in the 350 – 400 nm size domain with only few smaller particles (< 300 nm). On the other hand, the morphology of the Fe-$NC^{\Delta\text{-DCDA}}$ seems to be altered by DCDA-assisted activation from truncated polyhedron to partially irregularly shaped particles (Figs. 2b and S6). This morphological transformation of catalyst particles is attributed to the presence of DCDA, a commonly used "blowing agent" which generates nitrogen and ammonia during its decomposition at 300-350^{o}C and leaves a conductive carbon overlayer on top of the polyhedra particles during the activation step.[41,42] Fig. 2c shows high-angle annular dark-field scanning transmission electron microscopy (HAADF-STEM) image of the Fe-$NC^{\Delta\text{-DCDA}}$ along with iron mapping (Fig. 2c inset) by energy dispersive X-ray spectroscopy (EDXS). A uniform distribution of Fe is visible throughout the carbon matrix and the strong signal intensity reflects high Fe loading which was determined to be 7.10 wt% by ICP-MS (Table S2). Aberration-corrected HAADF-STEM micrographs of Fe-$NC^{\Delta\text{-DCDA}}$ catalyst represent Fe sites at atomic resolution (Figs. 2d-e and S8c-d). The presence of isolated bright spots throughout the carbon matrix indicates the existence of abundant atomic Fe sites which was confirmed by electron energy loss spectroscopy (EELS). The EELS spectrum (Fig. 2f) of the framed area of micrograph in Fig. 2d shows a clear Fe signal originating from the single iron atoms. The aberration-corrected HAADF-STEM micrographs of Fe-NC^{U} catalyst (Fig. S8a-b) reveal Fe atoms (along with the residual Zn) present in the form of isolated single atoms even before the activation step, with no metal clustering detected. The overall carbon-particle size distribution in the Fe-

$NC^{\Delta\text{-DCDA}}$ was estimated by multi-angle dynamic light scattering (MADLS) and majority of the particles/aggregates (85%) are found to be in 400 – 500 nm range, peaking at 450 nm, while the rest (15%) are smaller and cantered at 215 nm (Fig. 2g). Nitrogen functionalities were quantitatively and qualitatively evaluated by X-ray photoelectron spectroscopy (XPS). Total amount of doped nitrogen in the Fe-NC^{U} sample is found to be high with a value of 12.5 at%. This is favourable to stabilise large quantities of Fe ions and thus constructing Fe-N_X moieties by Lewis acid – Lewis base interactions. Deconvolution of the N 1s spectrum of this sample reveals that more than 97% of the doped nitrogen is present as pyridinic, metal-coordinated (M-N_X sites), and pyrrolic N sites (Figs. 2h and S9). Total nitrogen contents in the Fe-$NC^{\Delta\text{-DCDA}}$ and Fe-NC^{Δ} catalysts are 6.8 and 7.8 at%, respectively. As can be seen in Figs. 2h and S9, the catalyst activation results in a modified contribution of the different N groups. Particularly, the peak corresponding to pyrrolic N is increased in the Fe-$NC^{\Delta\text{-DCDA}}$ catalyst as compared to before activation (13.8 rel.% for Fe-NC^{U} *vs* 28.4 rel.% for Fe-$NC^{\Delta\text{-DCDA}}$) and a small N-oxide peak also emerges in the N 1s narrow-scan spectrum (Fig. S9). Like the unactivated sample, the majority (> 90%) of nitrogen in Fe-$NC^{\Delta\text{-DCDA}}$ exists as pyridinic, M-N_x, and pyrrolic N sites, while graphitic N and N-oxide values are only 6 and 3.5 %, respectively (Fig. S9). The distribution of different N sites in the Fe-NC^{Δ} sample is almost identical to that of the Fe-$NC^{\Delta\text{-DCDA}}$ indicating no distinguishable modification of nitrogen functionalities in the presence of DCDA during activation. A comparison of nitrogen adsorption-desorption isotherms (Fig. S10a) shows type I isotherms for all three samples with restricted hysteresis, indicating predominantly microporous structures. The specific surface areas (SSA) of the Fe-NC^{U}, Fe-NC^{Δ} and Fe-$NC^{\Delta\text{-DCDA}}$ determined by the BET method are 775, 1070, and 1155 $m^2\ g^{-1}$ respectively, while their respective micropore volumes are 0.277, 0.398, and 0.432 $cm^3\ g^{-1}$ (Fig. S10b and Table S3). The

considerable increase in SSAs and micropore volumes of the two activated catalysts is attributed to the evaporation of Zn during the activation step which decreased from around 5 wt% to < 1 wt% (Table S2). Compared to the control Fe-NC$^{\Delta}$ sample, the additional enhancement in SSA and micropore volume for the Fe-NC$^{\Delta\text{-DCDA}}$ catalyst is likely caused by the presence of DCDA during activation by altering the morphology of primary catalyst particles which lead to an improved active site accessibility/utilisation as discussed later.

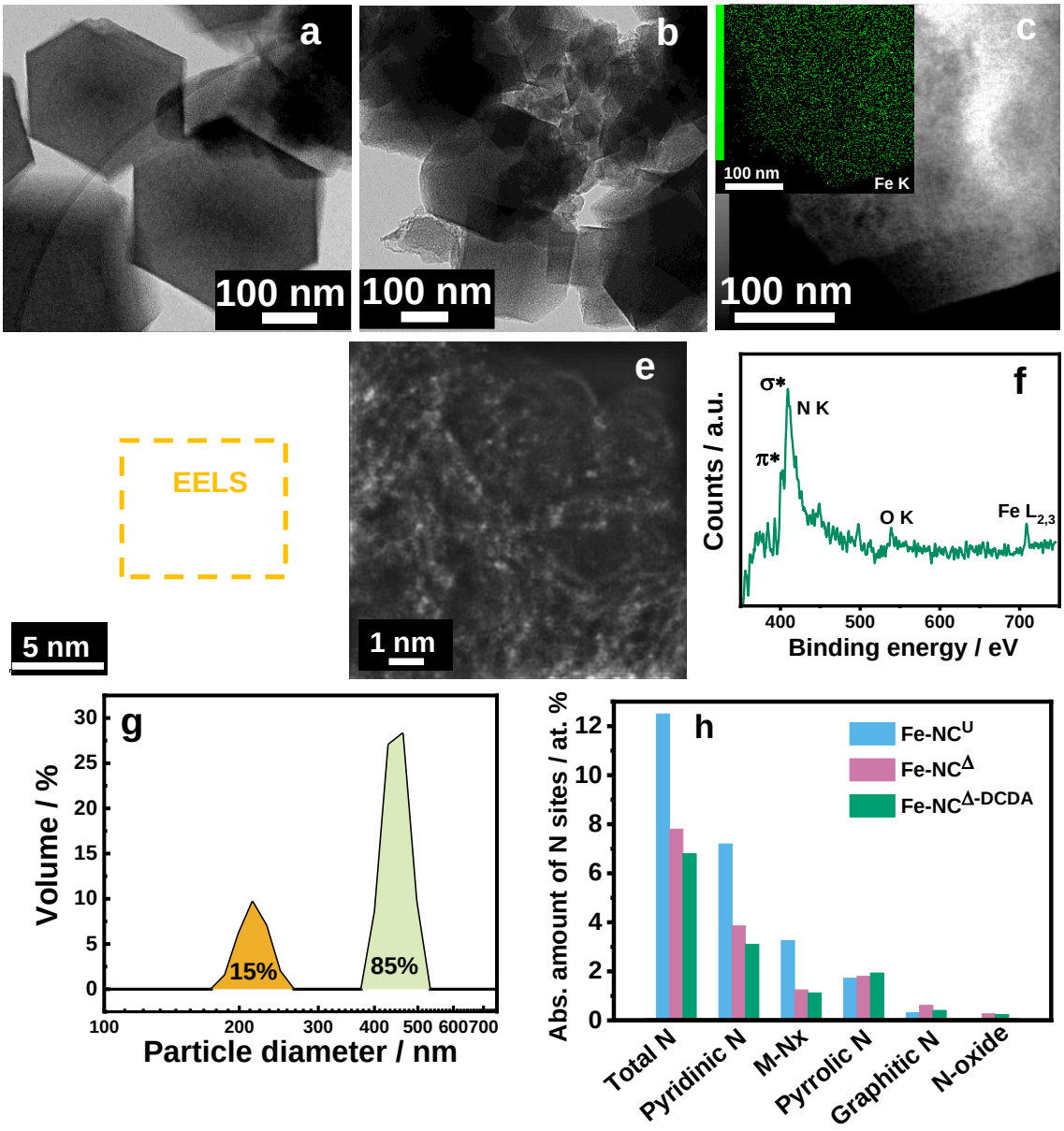

Fig. 2. Structural analysis of Fe-NC catalysts. TEM images of (a) Fe-NC^{U} and (b) Fe-NC$^{\Delta\text{-DCDA}}$; (c) HAADF-STEM image of Fe-NC$^{\Delta\text{-DCDA}}$ with inset showing Fe mapping by EDXS; (d & e) Aberration-corrected atomic resolution HAADF-STEM micrographs of Fe-NC$^{\Delta\text{-DCDA}}$; (f) EELS spectrum of framed area of micrograph in (d); (g) particle size distribution of the Fe-NC$^{\Delta\text{-DCDA}}$ determined by multi-angle dynamic light scattering (MADLS); (h) absolute amounts of total nitrogen and different N sites in the unactivated and activated Fe-NCs determined from the deconvoluted high resolution N 1s XPS spectra of those catalysts.[43]

Raman analysis of the Fe-NC$^{\Delta\text{-DCDA}}$ catalyst indicates graphene-like domains with sizes (L_a) of 7.3±2.3 nm (n=10) (supplementary note S2, Fig S11). We use value with the specific surface area of the catalyst to estimate the number of basal, edge and buried sites in the catalyst (supplementary note S1 and Table S1)

Evaluation of Fe coordination and Fe-N_x site formation: The Fe coordination and speciation before and after catalyst activation were investigated by XAS and cryostatic ^{57}Fe Mössbauer spectroscopy. XAS measurements were carried out at the various stages of the synthesis process, by collecting both the extended X-ray absorption fine structure (EXAFS) and the X-ray absorption near-edge structure (XANES) regions (supplementary note S3). The Fourier transform (FT) of the EXAFS spectrum of Zn-NC in the first synthesis step, clearly shows the features of single atomic zinc sites (Fig. S12a-b). The EXAFS analysis reveals a first coordination shell comprising four nitrogen atoms around Zn at 2.02 Å, and a second coordination shell due to Zn-C contribution at 3.19 Å. The structural parameters obtained from the fitting procedure are reported in supporting Table S4, and they are, within the statistical errors, in good agreement with our previous determination of Zn-N_4 moieties in ZIF-8 pyrolysed catalysts.[44] The EXAFS spectrum of Fe-NC^{U} can be accurately reproduced by a first coordination shell comprising four nitrogen atoms and two axial oxygen atoms around the iron, and a second coordination shell including Fe-C and Fe-Fe two body signal (Figs. 3a and S13, and

Table S4). As also evidenced by Mössbauer spectroscopy, in this step of the synthesis the EXAFS analysis reveals the coexistence of Fe-N_4 moieties and an iron-oxide phase. Moreover, the comparison between the XANES spectra of Fe-NC^U and γ-Fe_2O_3 and α-Fe_2O_3 allows to establish the presence of the α-Fe_2O_3 phase, because of the closer edge position and the same shape and position of the pre-edge peak (Fig. S14). The first shell and the Fe-Fe bond distances agree with the α-Fe_2O_3 crystallographic determination[45], while the low Fe-Fe coordination number is a consequence of the sub-nanometric size of Fe_2O_3 particles and the co-existence of Fe-N_4 sites. The EXAFS spectrum of the activated Fe-$NC^{\Delta\text{-DCDA}}$ catalyst can be correctly reproduced by a FeN_xC_y moiety with four nitrogen atoms at 2.02 Å and two Fe-C contributions in the higher coordination shells (Figs. 3b and S15, and Table S4). The Fe-N bond length is, within the estimated errors, in good agreement with our previous EXAFS determinations on Fe-NC pyrolysed catalysts.[46] In a recent study, we showed that only cryostatic ^{57}Fe Mössbauer spectroscopy could spectroscopically distinguish Fe-N_x sites from nano/amorphous iron oxides formed *in operando* during fuel cell testing of a Fe-NC material initially comprising of only Fe-N_x sites and being devoid of Fe-oxides.[47] ^{57}Fe Mössbauer spectroscopy was therefore conducted at 5 K to study the Fe speciation in Fe-NC before and after the activation. The spectrum of Fe-NC^U was fitted with a sextet component that can clearly be assigned to Fe_2O_3 and with a doublet (labelled D1*) with quadrupole splitting (QS) of 1.1 mm s^{-1} (Fig. 3c). The latter can be assigned either to a sub type of Fe-N_x sites.[10,31,48] or to superparamagnetic Fe oxide (it can be hypothesized that sub-nanometric or few atom clusters of Fe and O would remain superparamagnetic even at 5 K). The Fe-NC^U therefore contains both Fe-N_x-like sites and a significant fraction of Fe as Fe_2O_3. The Fe_2O_3 is presumably present at a sub-nanometer size domain (a few atoms of Fe and O) as no obvious iron clustering could be detected by atomic

resolution HAADF-STEM (Fig. S8a-b). Although a few pairs of heavy elements (bright spots) are apparent in Fig. S8b, suggesting the existence of binuclear M_2N_x sites[49], however those may be Fe (or Zn) single atoms embedded in two different layers of graphene sheets.

After the activation however, the sextet signal disappeared and the Mössbauer spectrum was fitted with mainly two doublets labelled D1 and D2 assigned to Fe-N_x moieties, and a minor signal of a third doublet (D3) (Fig. 3d). While the isomer shifts (IS) of D1 and D2 are similar, their QS values strongly differ, D1 having typically a QS close to 1 mm s^{-1} and D2 in the range of 1.9-2.6 mm s^{-1}. More precisely, D1 was recently identified from an *ex situ* experimental characterisation combined with DFT-calculation of the quadrupole splitting of Fe-N_x sites to be a ferric high-spin Fe-N_x moiety, with an oxygen adsorbate on top.[50] This assignment has been strengthened by the first *in situ* Mössbauer spectroscopy study in PEMFC, showing that D1 in another Fe-NC catalyst reversibly switched to a quadrupole doublet with isomer shift of *ca* 1 mm s^{-1} at low electrochemical potential, which can be unambiguously assigned to a high-spin ferrous species.[33] Doublet D2 is typically observed in pyrolysed Fe-NC samples, co-existing with D1, with exact D1/D2 ratio that depend on the synthesis.[20,46,48,50] From experimental *ex situ* characterisation coupled to DFT prediction of QS-values, D2 has recently been assigned to Fe-N_x moieties in ferrous state and with low or medium spin state.[50] Moreover, it was shown that the D2 signal is independent of the cathode potential and atmosphere (O_2-free or O_2-rich)[51], supporting the fact that it corresponds either to sites situated in the bulk of the carbon matrix, and/or to surface sites that bind O_2 weakly. The minor D3 component can be unambiguously assigned to high-spin ferrous centers, due to its high isomer shift of 1.04 mm s^{-1} (Table S5, supplementary note S4). It may correspond either to a third type of Fe-N_x sites.[48], or to $FeCl_2$ hydrate or graphite intercalated $FeCl_2$ (with IS values matching those of D3,[52,53]) remaining

from the activation step. A doublet with IS and QS values similar to those of D3 has been observed in the Mössbauer spectrum of a Fe-NC synthesised *via* non-contact pyrolysis of $FeCl_3$ and a nitrogen-doped carbon support, and assigned to $FeCl_2 \cdot 4H_2O$.[32] The main difference between the Mössbauer spectra of Fe-NC^U and Fe-$NC^{\Delta\text{-DCDA}}$ is therefore the conversion of all Fe_2O_3 magnetic particles (sextet component) into Fe-N_x sites (D1, D2). If a fraction of the D1* signal in the Fe-NC^U comes from superparamagnetic Fe-oxides, their conversion to Fe-N_x sites of type D1 would not be observable in the spectrum of the Fe-$NC^{\Delta\text{-DCDA}}$. The conversion from nano-Fe-oxides into Fe-N_x sites during pyrolysis has been recently and independently demonstrated by Wu's group [54] and by Jia's group [32]. In our recent work, it is observed that adsorption of oxygen at the Fe-N_x sites and subsequent spillover to the neighbouring carbon atoms results in the degradation of ORR activity which could then be recovered by activating the catalyst at 600 ^oC.[55] This may indicate a potential formation of iron oxo species/nanoxide by oxygen adsorption which could be reconverted to Fe-N_x sites by heat treatment.

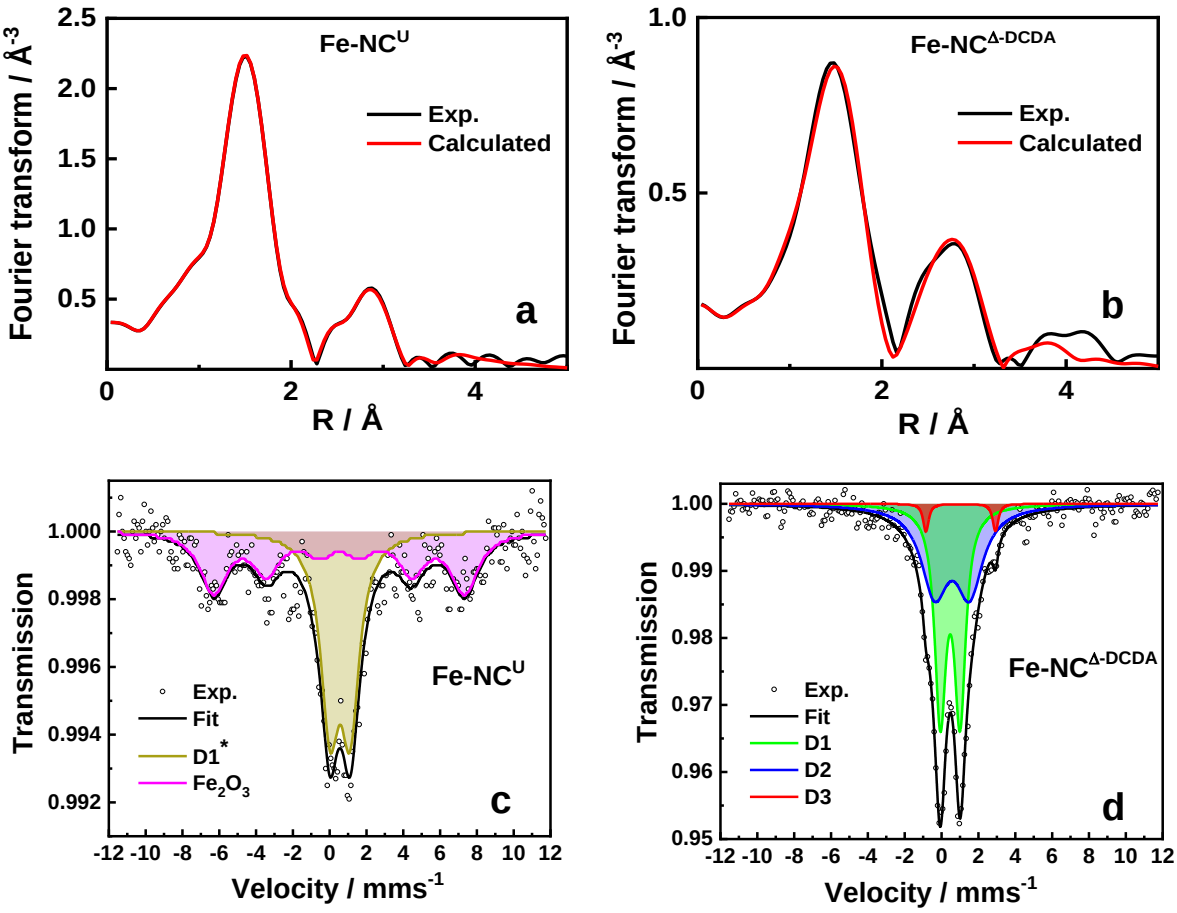

Fig. 3. Analysis of Fe coordination environment in Fe-NC catalysts before and after activation. Fe K-edge EXAFS analysis of (a) Fe-NC^{U} and (b) Fe-NC$^{\Delta\text{-DCDA}}$ in the Fourier transformed space without phase-shift correction. The black curves represent the experimental spectra, while the red curves represent the calculated spectra; ^{57}Fe cryo Mössbauer spectra measured at 5 K of (c) Fe-NC^{U} and (d) Fe-NC$^{\Delta\text{-DCDA}}$.

Determination of SD and TOF by nitrite and CO methods: In order to understand how this structural transformation of iron sites from the unactivated to activated Fe-NC impacts electrocatalytic features such as site density and site activity, *in situ* nitrite stripping technique was employed (Supplementary Note S5).[34] When the Fe-NC^{U} and Fe-NC$^{\Delta\text{-DCDA}}$ were probed by nitrite stripping, a large well-defined nitrite reduction peak is observed for the latter that can be witnessed in its poisoned cyclic voltammetry (CV) between 0.29 – -0.30 V_{RHE} (Fig. 4b), while only a tiny reductive peak current is observed in the corresponding CV of Fe-NC^{U} (Fig. 4a). The

total amount of charge associated with the NO stripping peak of Fe-NC$^{\Delta\text{-DCDA}}$ is 37.4 C g^{-1} (inset of Fig. 4b) which is over six times greater than 5.8 C g^{-1} for Fe-NC^{U} (inset of Fig. 4a). The corresponding SD values for the Fe-NC^{U} and Fe-NC$^{\Delta\text{-DCDA}}$ are 0.72 x 10^{19} sites g^{-1} (0.93 x 10^{16} sites m^{-2}) and 4.67×10^{19} sites g^{-1} (4.04 x 10^{16} sites m^{-2}), respectively (Fig. 4e). This SD value represents only about 7% of surface accessible iron based on Fig. 1a and involving the iron loading and the catalyst specific surface area (6% of total iron in the material), but is surprisingly close to the number of edge iron sites (6±2×10^{19} sites g^{-1}) estimated for this catalyst based on a domain size of L_a=7.3±2.3 nm (supplementary note S1 for calculation and Table S1). Thus, there is the potential to increase the mass activity of the catalyst by about a factor of 13 if all surface sites can achieve the same activity. This is qualitatively in line with the complete conversion of the sextet component assigned to Fe_2O_3 into doublets D1 and D2, assigned to FeN_x sites in the Fe-NC$^{\Delta\text{-DCDA}}$. One can however not exclude that a fraction of the D1* signal in Fe-NC^{U} came from superparamagnetic ferric oxide, that would likely have transformed to FeN_x sites during activation. In this case, the increase in SD from Fe-NC^{U} to Fe-NC$^{\Delta\text{-DCDA}}$ would be even stronger than expected based on the conversion of the sextet component (Fe_2O_3) into FeN_x during activation. It must also be noted that DCDA plays an important role in the enhanced SD value during activation, since the control Fe-NC$^{\Delta}$ sample showed an SD of only 1.12 x 10^{19} sites g^{-1}, lower than 4.67 x 10^{19} sites g^{-1} for Fe-NC$^{\Delta\text{-DCDA}}$ (Table S6, Fig. S17).

In addition to the *in situ* nitrite stripping method, *ex situ* CO cryo chemisorption technique was also employed for the determination of site densities (Fig. S19).[35,37] The calculated SD(CO) values for the Fe-NC^{U} and Fe-NC$^{\Delta\text{-DCDA}}$ are 4.86 x 10^{19} and 7.83 x 10^{19} sites g^{-1}, respectively (Fig. 4e). While the trend of SD values for both Fe-NCs are comparable for the CO and nitrite stripping techniques, the SD values determined by CO chemisorption are considerably higher (7

and 1.7 times for the unactivated and activated samples, respectively). Since CO cryo chemisorption is a gas phase method, it can probe more Fe-N_x sites than nitrite stripping, which requires accessibility of nitrite ions to the active sites *via* a liquid electrolyte. Thus, CO method presumably represents an upper bound while nitrite method represents a lower bound on the number of sites.[38] The 1.7 times higher SD(CO) *vs* SD(nitrite) for the Fe-$NC^{\Delta\text{-DCDA}}$ is in line with the previous differences observed among four pyrolysed Fe-NC samples.[38] For the Fe-NC^{U}, the difference of 7x between the two techniques is however significantly above what has been observed hitherto for highly ORR-active Fe-NC obtained after high temperature pyrolysis. This suggests that the Fe species present on the top surface (sub-nanometric Fe_2O_3 particles are known to be on top of the surface based on the synthesis protocol) in Fe-NC^{U} behaves differently with CO and nitrite from those in Fe-$NC^{\Delta\text{-DCDA}}$. While the nitrite stripping is liable to be more specific to Fe-N_x sites for "counting", it is possible that the CO method either counts the sub-nanometric Fe_2O_3 particles present in Fe-NC^{U} or alternatively, the sub-nanometric Fe_2O_3 is converted to Fe-N_x or Fe(0) sites during the cleaning step in reductive atmosphere at 600 °C that precedes the CO chemisorption measurement.

The intrinsic catalytic activity in terms of TOF was estimated from the decrease in ORR kinetic current upon nitrite poisoning, and dividing by SD(nitrite). Tafel plots for the ORR on these two catalysts were obtained by correcting the RDE polarisation curves for Ohmic and diffusion losses (Fig. 4c-d) showing the effect of poisoning of the catalyst (Fig. S16a-b for RDE responses). It is observed that the Fe-NC^{U} catalyst exhibits a low absolute ORR activity under nitrite stripping conditions (in acetate electrolyte at pH 5.2) and does not show any noticeable ORR performance loss when poisoned in the presence of nitrite (Figs. 4c and S16a). On the other hand, the Fe-$NC^{\Delta\text{-DCDA}}$ delivers a high ORR activity before poisoning and then undergoes a large

drop of ORR current after poisoning, which can be fully recovered by reductive stripping of NO (Figs. 4c and S16b). The derived $TOF_{5.2}$ (the subscript represents electrolyte pH 5.2 at which TOF is estimated) was assessed at 0.80, 0.85 and 0.90 V_{RHE}. The $TOF_{5.2}$ value of 0.054 electrons $site^{-1}$ s^{-1} was calculated at 0.80 V_{RHE} for the unactivated sample and could not be assessed at higher potential (Fig. 4f). The calculated $TOF_{5.2}$ values for the Fe-$NC^{\Delta\text{-DCDA}}$ catalyst at 0.80, 0.85 and 0.90 V_{RHE} are 1.12, 0.13 and 0.02 electrons $site^{-1}$ s^{-1}, respectively (Fig. 4f). Thus, by comparing the $TOF_{5.2}$ values of the two catalysts at 0.80 V_{RHE} (0.054 and 1.12, i.e. x21 improvement), it becomes clear that the activation step plays a key role not only in improving the SD (x6.5, Table S6) but even more importantly in improving the TOF of electrochemically accessible Fe-sites detected in the Fe-NC^{U} by nitrite stripping.

The advancement made in the SD and $TOF_{5.2}$ levels in the present work is gauged against four Fe-NC catalysts that have been benchmarked in our recent work under CRESCENDO project.[38] Isoactivity plots are drawn using SD and $TOF_{5.2}$ values (at 0.80 and 0.85 V_{RHE}) to compare the Fe-$NC^{\Delta\text{-DCDA}}$ with benchmark catalysts. The four benchmark Fe-NCs were developed in different laboratories and are labelled as CNRS (ZIF-derived catalyst from CNRS/University of Montpellier), UNM (silica templating based catalyst from University of New Mexico), ICL (polymerised di-amino naphthalene-based catalyst from Imperial College London which is a reference Fe-NC catalyst in our laboratory), and PAJ (commercial catalyst from Pajarito Powder Inc. with product name PMF-011904). From Fig. 4g-h, it can be seen that the Fe-$NC^{\Delta\text{-DCDA}}$ possesses an exceptionally high SD, with improvement ranging between 3-18 fold when compared to the four state-of-the-art catalysts. Compared to the ZIF-derived CNRS benchmark catalyst that was optimised for increased SD, the Fe-$NC^{\Delta\text{-DCDA}}$ contains not only more than 3x density of active sites but also higher $TOF_{5.2}$ values. At 0.80 V_{RHE}, $TOF_{5.2}$ of the Fe-$NC^{\Delta\text{-DCDA}}$

catalyst is 1.12 electrons site^{-1} s^{-1} that is > 1.7x greater than 0.65 electrons site^{-1} s^{-1} for the CNRS catalyst. Among the four benchmark materials, the PAJ catalyst had the lowest SD (0.25 x 10^{19} sites g^{-1}) but highest $TOF_{5.2}$ (7.23 electrons site^{-1} s^{-1} at 0.80 V_{RHE}). The present Fe-NC$^{\Delta\text{-DCDA}}$ catalyst combines successfully highest SD and relatively high TOF, leading to impressive ORR mass activity.

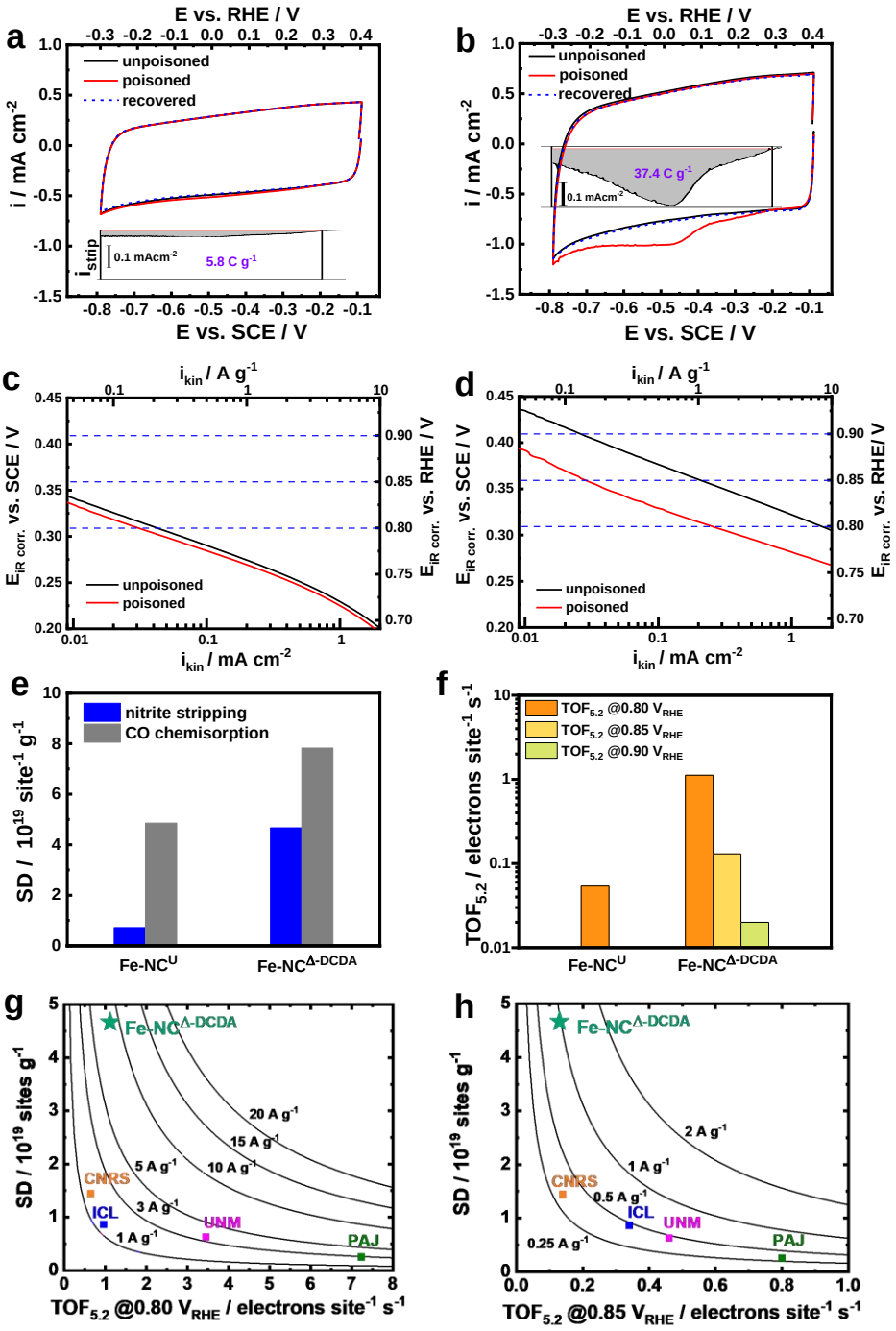

Fig. 4. Site density and turnover frequency measurement of Fe-NC catalysts in pH 5.2 electrolyte. CVs of (a) Fe-NC^{U} and (b) Fe-NC$^{\Delta\text{-DCDA}}$ catalysts at unpoisoned, poisoned and recovered stages of nitrite stripping protocol. Inset shows the amount of charge associated with the reduction of nitrite molecules adsorbed on Fe sites; negative shift of kinetic ORR activities of (c) Fe-NC^{U} and (d) Fe-NC$^{\Delta\text{-DCDA}}$ upon nitrite poisoning; (e) comparison of site density values determined by nitrite stripping and CO chemisorption methods for both catalysts; (f) comparison of turnover frequencies ($TOF_{5.2}$) at 0.80, 0.85 and 0.90 V_{RHE} for both catalysts; isoactivity plots at (g) 0.80 V_{RHE} and (h) 0.85 V_{RHE} comparing the ORR performance metric of Fe-NC$^{\Delta\text{-DCDA}}$

catalyst developed in this study to recently reported four benchmark Fe-NCs.[38] The nitrite stripping measurements were performed in 0.5 M acetate buffer electrolyte (pH 5.2) at 1600 rpm and the catalyst loading was 0.2 mg cm^{-2}.

ORR activity and SD – ORR correlation: The ORR activity of Fe-NC catalysts was also evaluated in more acidic conditions using 0.5 M H_2SO_4 electrolyte (pH 0.3). In addition to the Fe-NC^{U}, Fe-$NC^{\Delta\text{-DCDA}}$, and Fe-NC^{Δ} catalysts, an additional Fe-$NC^{\Delta\text{-CA}}$ sample was synthesised by replacing the DCDA with cyanamide (CA) during the activation step to assess the effect of SD and TOF on ORR performance. As shown in Fig. 5a, ORR voltammetry demonstrates high ORR performance in the order of Fe-$NC^{\Delta\text{-DCDA}}$ > Fe-$NC^{\Delta\text{-CA}}$ > Fe-NC^{Δ} > Fe-NC^{U}. The best performing Fe-$NC^{\Delta\text{-DCDA}}$ catalyst delivers an outstanding activity with a half-wave potential ($E_{1/2}$) of 0.815 V_{RHE} at a low loading of 0.2 mg cm^{-2} and mass activities of 31.9 A g^{-1} at 0.80 V_{RHE} and 4.9 A g^{-1} at 0.85 V_{RHE}, which are far greater than the respective highest values obtained for the benchmark Fe-NCs (Fig. S20).

Although we have previously shown that the site activity is pH independent between pH 0.3 and 5.2 for our benchmark Fe-NC catalyst[34], it is unclear whether this is a universal effect for all Fe-NCs. Hence, we use the total kinetic current measured at pH 0.3 (*i.e.* the same approach used when estimating site activity from CO chemisorption) to establish an alternative TOF (labelled as $TOF_{0.3}$) from the combination of nitrite SD measurement at pH 5.2 and ORR activity measurement in sulfuric acid at pH 0.3. The ORR kinetic mass activities at pH 0.3 of the activated Fe-NCs show linear correlation with mass-based SD (sites g^{-1}) (Fig. 5b). In addition, the trend of ORR improvement is almost identical for both mass-based and surface area-based values of SD (Figs. 5b, S24 and S25), suggesting the active sites are strongly correlated with surface as might be expected. It is also intriguing that the plots point to a zero intercept at non-zero site density – this implies that for these catalysts, there is a minimum acceptable site density

below which there is no appreciable activity. The lines which fit the datapoints are established by fitting all the data points to the function

$$j(\eta, SD) = (SD - SD_0)\, q_e\, j_{o,site} exp\left(\frac{-\alpha\eta F}{RT}\right) \qquad \text{Equation 2}$$

Where j is the mass activity (A g^{-1}) and is a function of the overpotential (η, V) and the site density (SD, sites g^{-1}), SD_0 is the minimum number of sites required before we see any activity (A g^{-1}), $j_{o,site}$ is the exchange current density associated for a single site in terms of turnover frequencies (electrons $site^{-1}$ s^{-1}), and q_e is the charge on an electron. In order to take the overpotential into account, we apply the Tafel approximation as we are >> $\frac{4RT}{F}$ V away from the equilibrium potential. Hence, we include the overpotential (the potential difference between the potential applied and the equilibrium potential of oxygen reduction, 1.229 V) multiplied by the symmetry factor (α), Faraday constant (F, C mol^{-1}), and the temperature and gas constant (T, K and R, 8.314 J K^{-1} mol^{-1}). Equation 2 was fit to all datapoints in Fig. 5b simultaneously, using as fitting parameters $SD_0, j_{o,site}$ and α using a fitting procedure which samples the parameter space to arrive at a statistically likely global best fit (further details in the supplementary note S6). The best fit parameters are SD_0 = 6.2×10^{18} sites g^{-1}; $j_{o,site}$ = 5.0×10^{-7} electrons $site^{-1}$ s^{-1} and α=0.96. A non-zero value of SD_0 implies that across the catalysts tested, there is a constant number of sites which do not contribute to the electrochemical current and it is only when we have more than this number of sites do we see any significant ORR activity. This might be due to the nitrite stripping approach overcounting the number of active sites, which may imply that certain number of sites are active for the nitrite adsorption and reduction but inactive for the ORR. The surprising result is that we can replicate all the data assuming a single type of site with a consistent variation of activity. It is useful to compare the value of $j_{o,site}$ to what would be expected for platinum. Using the data on the exchange current density for 2.48 nm platinum

particles[56], we calculate a $j_{o,site}$ for platinum of 0.012 electrons site$_{Pt}^{-1}$ s^{-1} at the equilibrium potential (where we count each surface platinum atom as a "site"). Hence, surface platinum atoms in platinum nanoparticles are about 20,000 fold more active than the Fe-NC sites at the equilibrium potential. However, the improvement in activity of the Fe-NC sites is associated with a low Tafel slope of 61 mV decade^{-1} meaning that the Fe-NC sites increase in activity faster than Pt for which much higher Tafel slopes (~137 mV decade^{-1} outside the oxide region[56]) are typically measured. The Fe-NC sites have a TOF$_{0.3}$ (turnover frequency at pH 0.3) of 0.10, 0.84 and 5.4 electrons site^{-1} s^{-1} at 0.90, 0.85 and 0.80 V$_{RHE}$, respectively (Table S7), significantly greater (≥ 5x) than TOF$_{5.2}$ values (measured at pH 5.2) in Fig. 4.

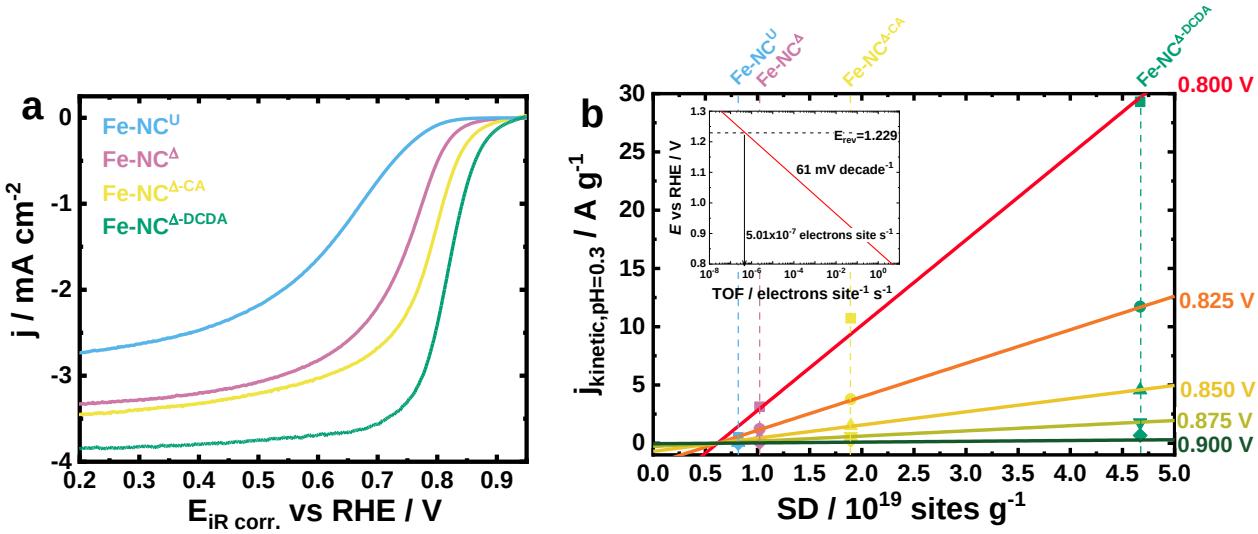

Fig. 5. ORR activities and correlations with SD and kinetic activity in pH 0.3 electrolyte. (a) RDE ORR curves measured in O_2-saturated 0.5 M H_2SO_4 at 5 mV s^{-1} with a rotation speed of 900 rpm. Catalyst loading was 0.2 mg cm^{-2}; (b) Correlation of kinetic ORR activity in 0.5 M H_2SO_4 at different potentials with mass-based SD measured by nitrite stripping. Lines represent the fit to equation 2. Inset represents a plot of the derived activity of the sites in all catalysts showing the activity at the equilibrium potential and the Tafel slope determined from the plot.

The selectivity of Fe-NC$^{\Delta\text{-DCDA}}$ towards four-electron oxygen reduction pathway was determined by measuring the peroxide yields at three different loadings (0.1, 0.2 and 0.8 mg cm^{-2}). A relatively low H_2O_2 yield is detected at all loadings which remains between 1-2% across the

wide potential range (Fig. S26), indicating that Fe-N_4 sites are predominantly catalysing the ORR by four-electron mechanism.

Performance characterisation in fuel cell: Single cell PEMFC tests were carried out in 5 cm^2 and 50 cm^2 (Supplementary Note S8) cell active area with Fe-$NC^{\Delta\text{-DCDA}}$ as the cathode catalyst (3.9 mg cm^{-2} loading; 1.0 mg cm^{-2} in large area configuration to ameliorate mass transport effects – see introduction) under both oxygen and air environments at 80 ^oC at 1 bar gauge pressure and 100% relative humidity (RH) at both electrodes (Figs. 6 and S27-36). Under H_2-O_2 conditions, the catalyst delivers an excellent performance with a current density of 41.3 mA cm^{-2} at the reference cell voltage of 0.90 $V_{iR\text{-free}}$ (Fig. 6a), which is amongst highest ever reported values for PGM-free catalysts.[6,20,22,26,33,40,46,57] This translates into a mass activity of 10.6 A g^{-1} reflecting the high kinetic activity of our catalyst. Recently, current densities in 25 – 33 mA cm^{-2} range have been reported at 0.90 $V_{iR\text{-free}}$ but mostly with ultra-high Fe-NC loadings (6.0 – 6.8 mg cm^{-2})[33,40], resulting in low mass activities between 4 – 6 A g^{-1}. The substantial progress in the kinetic current density of Fe-NC catalyst accomplished in this work is compared with the best reported Fe-NC performances in Fig. 6c. In the high current density range, the fuel cell performs very well with a measured current density of 1130 mA cm^{-2} at 0.60 V (or 1910 mA cm^{-2} at 0.60 $V_{iR\text{-free}}$) and reaches an iR-corrected peak power density > 1.2 W cm^{-2} at a cell voltage of 0.49 $V_{iR\text{-free}}$ (Fig. S27). In H_2-air operation (Fig. 6b), the measured current density at reference voltage of 0.80 V is 145 mA cm^{-2} (or 199 mA at 0.80 $V_{iR\text{-free}}$), which is significantly higher than most of the previously reported values that ranged between 75 – 113 mA cm^{-2}. [6,20,22,26,40,57-59] A measured current density of 700 mA cm^{-2} is reached at 0.6 V (or 805 mA cm^{-2} at 0.60 $V_{iR\text{-free}}$) (Figs. 6b and S29).

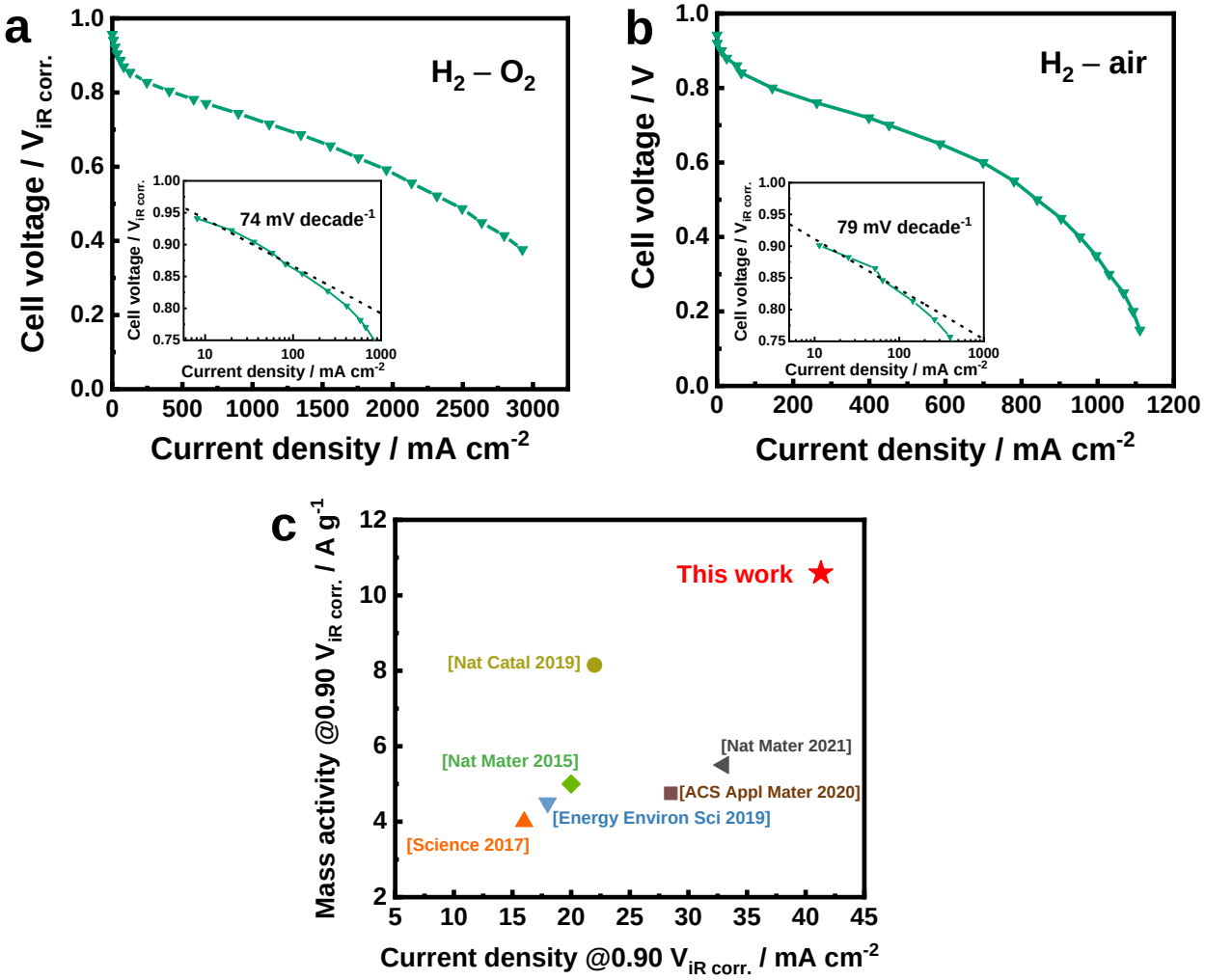

Fig. 6. Performance characterisation of Fe-NC$^{\Delta\text{-DCDA}}$ as cathode catalyst in a single cell PEMFC. (a) H_2-O_2 and (b) H_2-air polarisation curves; (c) comparison of current density and catalyst mass activity of Fe-NC$^{\Delta\text{-DCDA}}$ at reference voltage of 0.90 $V_{iR\text{-free}}$ under H_2-O_2 conditions with the best reported values. Test conditions: anode: commercial Pt/C anode with 0.4 mg_{Pt} cm^{-2} (Alfa Aesar, Johnson Matthey); cathode: Fe-NC$^{\Delta\text{-DCDA}}$ with 3.90 mg cm^{-2} loadings; Nafion® 211 membrane, cell temperature = 80 °C; 100% RH at both electrodes. Flow rates of 200 sccm of both gases for H_2-O_2 tests, and 300 and 1000 sccm of hydrogen and air, respectively, for H_2-air tests; 1 bar gauge pressure at both electrodes.

A peak power density of 429 mW cm^{-2} is obtained in H_2-air conditions at 0.55 V (483 mW cm^{-2} at 0.62 $V_{iR\text{-free}}$) (Fig. S29). Recently, it has been shown that the fuel cell performance of Fe-NCs, particularly in high current density region, is very sensitive to the mass-transport properties of

catalyst layer and can be improved by decreasing the catalyst particle size to 50 – 100 nm range[6,26,40,60], which indicates that further optimisation of primary catalyst particle size and cathode layer structure could potentially lead to even higher performance levels. Short stability tests were carried out in constant voltage mode at 0.40, 0.70 and 0.80 V in H_2-air environment(Fig. S32). The Fe-NC catalyst exhibits a relatively higher performance stability at 0.40 V with around 68% retention of initial current density after 10 hours as compared to 40-45% current density retention observed at higher operating voltage of 0.70 − 0.80 V. These results are consistent with the other studies where increased degradation rates were reported for high operating voltages caused by demetallation of Fe-N_4 sites and H_2O_2-induced carbon oxidation.[61,62] Electrodes were also compared before and after the stability tests through in situ cyclic voltammograms under nitrogen, electrochemical impedance spectroscopy (eis), and XANES (supplementary figures s33-s35). The voltammetry indicates an increase in pseudocapacitance, after fuel cell operation indicative of some corrosion and oxidation of the carbon (supplementary figure s33). The eis (supplementary figure s34) show significant increase in the charge transfer resistance after polarisation. The XANES analysis of Fe-NC cathodes before and after stability tests show some mobilisation of iron which enters the nafion electrolyte. This degradation highlights the need of stability improvement for Fe-NC catalysts specially at high operating voltages.

From these results, it becomes clear that with an exceptionally high atomic iron content (7 wt%), Fe-NC catalyst derived from a commercially produced ZIF-8 material could deliver an excellent fuel cell performance both in RDE as well as in single cell PEMFC tests.

Conclusions: A highly active Fe-NC catalyst has been developed from a Zn-N_x enriched NC matrix by exchanging Zn with Fe. The resultant activated Fe-NC catalyst consisted of 7 wt% iron

that is exclusively coordinated as Fe-N_4 sites as identified by ^{57}Fe Mössbauer spectroscopic measurements performed at 5 K, and XAS. The activation step played a key role in completely converting the nano-Fe-oxides into D1 and D2 sites. The Fe-$NC^{\Delta\text{-DCDA}}$ catalyst consisted of high SD values of 4.67 x 10^{19} and 7.8 x 10^{19} sites g^{-1} as determined by nitrite stripping and CO chemisorption methods, respectively, which are 3 – 18x greater than the benchmark Fe-NCs. This catalyst delivered an excellent ORR activity in RRDE with a mass activity of 31.9 A g^{-1} at 0.80 V_{RHE}. In PEMFC tests, an impressive performance is obtained with Fe-$NC^{\Delta\text{-DCDA}}$ catalyst with a current density of 41.3 mA cm^{-2} at 0.90 $V_{iR\text{-free}}$ in H_2-O_2 and 145 mA cm^{-2} at 0.80 V (or 199 mA at 0.80 $V_{iR\text{-free}}$) with a maximum power density of 429 mW cm^{-2} at 0.55 V in H_2-air environments. The synthesis strategy presented in this work can potentially overcome many hurdles that could be encountered with other complicated synthesis routes for mass producing Fe-NCs.

References

1 Fuel Cells and Hydrogen 2 Joint Undertaking. *Hydrogen Roadmap Europe*, <https://www.fch.europa.eu/sites/default/files/Hydrogen%20Roadmap%20Europe_Report.pdf> (2019).

2 Fuel Cell Technologies Office. *Multi-Year Research Development, and Demonstration Plan: Section 3.4 Fuel Cells, Office of Energy Efficiency and Renewable Energy*, <https://www.energy.gov/sites/prod/files/2017/05/f34/fcto_myrdd_fuel_cells.pdf> (2016).

3 Wilson, A., Kleen, G. & Papageorgopoulos, D. Fuel Cell System Cost - 2017. (DOE Hydrogen and Fuel Cells Program, 2017).

4 Jaouen, F. *et al.* Recent advances in non-precious metal catalysis for oxygen-reduction reaction in polymer electrolyte fuel cells. *Energy & Environmental Science* **4**, 114-130 (2011).

5 Jaouen, F. *et al.* Toward platinum group metal-free catalysts for hydrogen/air proton-exchange membrane fuel cells. *Johnson Matthey Technol. Rev* **62**, 231-255 (2018).

6 Chung, H. T. *et al.* Direct atomic-level insight into the active sites of a high-performance PGM-free ORR catalyst. *Science* **357**, 479-484 (2017).

7 Lefèvre, M., Proietti, E., Jaouen, F. & Dodelet, J.-P. Iron-based catalysts with improved oxygen reduction activity in polymer electrolyte fuel cells. *science* **324**, 71-74 (2009).
8 Wu, G., More, K. L., Johnston, C. M. & Zelenay, P. High-performance electrocatalysts for oxygen reduction derived from polyaniline, iron, and cobalt. *Science* **332**, 443-447 (2011).
9 Tylus, U. *et al.* Elucidating oxygen reduction active sites in pyrolyzed metal–nitrogen coordinated non-precious-metal electrocatalyst systems. *The Journal of Physical Chemistry C* **118**, 8999-9008 (2014).
10 Sahraie, N. R. *et al.* Quantifying the density and utilization of active sites in non-precious metal oxygen electroreduction catalysts. *Nature communications* **6**, 1-9 (2015).
11 Jasinski, R. A new fuel cell cathode catalyst. *Nature* **201**, 1212-1213 (1964).
12 Jasinski, R. Cobalt phthalocyanine as a fuel cell cathode. *Journal of the Electrochemical Society* **112**, 526 (1965).
13 Gupta, S., Tryk, D., Bae, I., Aldred, W. & Yeager, E. Heat-treated polyacrylonitrile-based catalysts for oxygen electroreduction. *Journal of applied electrochemistry* **19**, 19-27 (1989).
14 Martinez, U., Babu, S. K., Holby, E. F. & Zelenay, P. Durability challenges and perspective in the development of PGM-free electrocatalysts for the oxygen reduction reaction. *Current Opinion in Electrochemistry* **9**, 224-232 (2018).
15 Malko, D., Lopes, T., Symianakis, E. & Kucernak, A. The intriguing poison tolerance of non-precious metal oxygen reduction reaction (ORR) catalysts. *Journal of Materials Chemistry A* **4**, 142-152 (2016).
16 Kramm, U. I. *et al.* On an easy way to prepare metal–nitrogen doped carbon with exclusive presence of MeN4-type sites active for the ORR. *Journal of the American Chemical Society* **138**, 635-640 (2016).
17 Ranjbar Sahraie, N., Paraknowitsch, J. P., Göbel, C., Thomas, A. & Strasser, P. Noble-metal-free electrocatalysts with enhanced ORR performance by task-specific functionalization of carbon using ionic liquid precursor systems. *Journal of the American Chemical Society* **136**, 14486-14497 (2014).
18 Serov, A., Artyushkova, K. & Atanassov, P. Fe-N-C Oxygen Reduction Fuel Cell Catalyst Derived from Carbendazim: Synthesis, Structure, and Reactivity. *Advanced Energy Materials* **4**, 1301735 (2014).
19 Zhang, H. *et al.* Single atomic iron catalysts for oxygen reduction in acidic media: particle size control and thermal activation. *Journal of the American Chemical Society* **139**, 14143-14149 (2017).
20 Zhang, H. *et al.* High-performance fuel cell cathodes exclusively containing atomically dispersed iron active sites. *Energy & Environmental Science* **12**, 2548-2558 (2019).
21 Ferrandon, M. *et al.* Multitechnique characterization of a polyaniline–iron–carbon oxygen reduction catalyst. *The Journal of Physical Chemistry C* **116**, 16001-16013 (2012).
22 Wan, X. *et al.* Fe–N–C electrocatalyst with dense active sites and efficient mass transport for high-performance proton exchange membrane fuel cells. *Nature Catalysis* **2**, 259-268 (2019).
23 Liu, M., Liu, J., Li, Z., Song, Y. & Wang, F. A silica-confined strategy for completely atomic level Fe (II)-NC catalysts with a non-planar structure toward oxygen reduction reaction. *Journal of Catalysis* **370**, 21-29 (2019).

24 He, Y. *et al.* Highly active atomically dispersed CoN 4 fuel cell cathode catalysts derived from surfactant-assisted MOFs: carbon-shell confinement strategy. *Energy & Environmental Science* **12**, 250-260 (2019).

25 Hu, B.-C. *et al.* SiO 2-protected shell mediated templating synthesis of Fe–N-doped carbon nanofibers and their enhanced oxygen reduction reaction performance. *Energy & Environmental Science* **11**, 2208-2215 (2018).

26 He, Y., Liu, S., Priest, C., Shi, Q. & Wu, G. Atomically dispersed metal–nitrogen–carbon catalysts for fuel cells: advances in catalyst design, electrode performance, and durability improvement. *Chemical Society Reviews* (2020).

27 Das, R., Pachfule, P., Banerjee, R. & Poddar, P. Metal and metal oxide nanoparticle synthesis from metal organic frameworks (MOFs): finding the border of metal and metal oxides. *Nanoscale* **4**, 591-599 (2012).

28 Morozan, A., Goellner, V., Nedellec, Y., Hannauer, J. & Jaouen, F. Effect of the transition metal on metal–nitrogen–carbon catalysts for the hydrogen evolution reaction. *Journal of the Electrochemical Society* **162**, H719 (2015).

29 Ellingham, H. J. T. Reducibility of oxides and sulfides in metallurgical processes. *J Soc Chem Ind* **63**, 125-133 (1944).

30 Mehmood, A. *et al.* Facile Metal Coordination of Active Site Imprinted Nitrogen Doped Carbons for the Conservative Preparation of Non-Noble Metal Oxygen Reduction Electrocatalysts. *Advanced Energy Materials* **8**, 1701771 (2018).

31 Menga, D. *et al.* Active-Site Imprinting: Preparation of Fe–N–C Catalysts from Zinc Ion–Templated Ionothermal Nitrogen-Doped Carbons. *Advanced Energy Materials* **9**, 1902412 (2019).

32 Li, J. *et al.* Evolution Pathway from Iron Compounds to Fe1 (II)–N4 Sites through Gas-Phase Iron during Pyrolysis. *Journal of the American Chemical Society* **142**, 1417-1423 (2019).

33 Jiao, L. *et al.* Chemical vapour deposition of Fe–N–C oxygen reduction catalysts with full utilization of dense Fe–N4 sites. *Nature Materials*, 1-7 (2021).

34 Malko, D., Kucernak, A. & Lopes, T. In situ electrochemical quantification of active sites in Fe–N/C non-precious metal catalysts. *Nature communications* **7**, 1-7 (2016).

35 Luo, F. *et al.* Accurate evaluation of active-site density (SD) and turnover frequency (TOF) of PGM-free metal–nitrogen-doped carbon (MNC) electrocatalysts using CO cryo adsorption. *ACS Catalysis* **9**, 4841-4852 (2019).

36 Malko, D., Kucernak, A. & Lopes, T. Performance of Fe–N/C Oxygen Reduction Electrocatalysts toward NO2–, NO, and NH2OH Electroreduction: From Fundamental Insights into the Active Center to a New Method for Environmental Nitrite Destruction. *Journal of the American Chemical Society* **138**, 16056-16068, doi:http://dx.doi.org/10.1021/jacs.6b09622 (2016).

37 Leonard, N. D. *et al.* Deconvolution of utilization, site density, and turnover frequency of Fe–nitrogen–carbon oxygen reduction reaction catalysts prepared with secondary N-precursors. *ACS Catalysis* **8**, 1640-1647 (2018).

38 Primbs, M. *et al.* Establishing reactivity descriptors for platinum group metal (PGM)-free Fe–N–C catalysts for PEM fuel cells. *Energy & Environmental Science* **13**, 2480-2500, doi:10.1039/D0EE01013H (2020).

39 Osmieri, L. *et al.* Status and Challenges for the application of platinum group metal-free catalysts in proton exchange membrane fuel cells. *Current Opinion in Electrochemistry* (2020).
40 Uddin, A. *et al.* High Power Density Platinum Group Metal-free Cathodes for Polymer Electrolyte Fuel Cells. *ACS Applied Materials & Interfaces* **12**, 2216-2224 (2019).
41 Gupta, S. *et al.* Engineering Favorable Morphology and Structure of Fe-N-C Oxygen-Reduction Catalysts through Tuning of Nitrogen/Carbon Precursors. *ChemSusChem* **10**, 774-785 (2017).
42 Terrell, E. & Garcia-Perez, M. Application of nitrogen-based blowing agents as an additive in pyrolysis of cellulose. *Journal of Analytical and Applied Pyrolysis* **137**, 203-211 (2019).
43 Artyushkova, K. Misconceptions in interpretation of nitrogen chemistry from x-ray photoelectron spectra. *Journal of Vacuum Science & Technology A: Vacuum, Surfaces, and Films* **38**, 031002 (2020).
44 Li, J. *et al.* Volcano trend in electrocatalytic CO2 reduction activity over atomically dispersed metal sites on nitrogen-doped carbon. *ACS Catalysis* **9**, 10426-10439 (2019).
45 Wyckoff, R. W. G. *Crystal structures*. (John Wiley, New York, 1963).
46 Zitolo, A. *et al.* Identification of catalytic sites for oxygen reduction in iron-and nitrogen-doped graphene materials. *Nature materials* **14**, 937-942 (2015).
47 Li, J. *et al.* Identification of durable and non-durable FeNx sites in Fe–N–C materials for proton exchange membrane fuel cells. *Nature Catalysis* **4**, 10-19 (2021).
48 Kramm, U. I., Lefèvre, M., Larouche, N., Schmeisser, D. & Dodelet, J.-P. Correlations between mass activity and physicochemical properties of Fe/N/C catalysts for the ORR in PEM fuel cell via 57Fe Mossbauer spectroscopy and other techniques. *Journal of the American Chemical Society* **136**, 978-985 (2014).
49 Kneebone, J. L. *et al.* A Combined Probe-Molecule, Mössbauer, Nuclear Resonance Vibrational Spectroscopy, and Density Functional Theory Approach for Evaluation of Potential Iron Active Sites in an Oxygen Reduction Reaction Catalyst. *The Journal of Physical Chemistry C* **121**, 16283-16290 (2017).
50 Mineva, T. *et al.* Understanding Active Sites in Pyrolyzed Fe–N–C Catalysts for Fuel Cell Cathodes by Bridging Density Functional Theory Calculations and 57Fe Mössbauer Spectroscopy. *ACS Catalysis* **9**, 9359-9371 (2019).
51 Jing, M. *et al.* A feasible strategy to enhance mass transfer property of carbon nanofibers electrode in vanadium redox flow battery. *Electrochimica Acta* **390**, doi:10.1016/j.electacta.2021.138879 (2021).
52 Birchall, T. An investigation of some iron halide complexes by Mössbauer spectroscopy. *Canadian Journal of Chemistry* **47**, 1351-1354 (1969).
53 Wang, Z. & Inagaki, M. Moessbauer study of iron chloride-graphite intercalation compounds synthesized in molten salt. *Carbon* **29**, 423-427 (1991).
54 Li, J. *et al.* Thermally driven structure and performance evolution of atomically dispersed FeN4 sites for oxygen reduction. *Angewandte Chemie International Edition* **58**, 18971-18980 (2019).
55 Boldrin, P. *et al.* Deactivation, reactivation and super-activation of Fe-N/C oxygen reduction electrocatalysts: Gas sorption, physical and electrochemical investigation using NO and O2. *Applied Catalysis B: Environmental* **292**, 120169 (2021).
56 Zalitis, C. M., Kucernak, A. R. J., Lin, X. & Sharman, J. D. B. Electrochemical Measurement of Intrinsic Oxygen Reduction Reaction Activity at High Current Densities

as a Function of Particle Size for Pt4-xCox /C (x=0,1,3) Catalysts. *ACS Catalysis* **10**, 4361–4376, doi:10.1021/acscatal.9b04750 (2020).
57 Al-Zoubi, T. *et al.* Preparation of Nonprecious Metal Electrocatalysts for the Reduction of Oxygen Using a Low-Temperature Sacrificial Metal. *Journal of the American Chemical Society* **142**, 5477-5481 (2020).
58 Li, J. *et al.* Structural and mechanistic basis for the high activity of Fe–N–C catalysts toward oxygen reduction. *Energy & Environmental Science* **9**, 2418-2432 (2016).
59 Xie, X. *et al.* Performance enhancement and degradation mechanism identification of a single-atom Co–N–C catalyst for proton exchange membrane fuel cells. *Nature Catalysis* **3**, 1044-1054 (2020).
60 Banham, D. *et al.* Critical advancements in achieving high power and stable nonprecious metal catalyst–based MEAs for real-world proton exchange membrane fuel cell applications. *Science advances* **4**, eaar7180 (2018).
61 Chenitz, R. *et al.* A specific demetalation of Fe–N 4 catalytic sites in the micropores of NC_Ar+ NH 3 is at the origin of the initial activity loss of the highly active Fe/N/C catalyst used for the reduction of oxygen in PEM fuel cells. *Energy & Environmental Science* **11**, 365-382 (2018).
62 Gao, Y. *et al.* New insight into effect of potential on degradation of Fe-NC catalyst for ORR. *Frontiers in Energy* (2021).

Acknowledgments:

This work was funded by the Fuel Cells and Hydrogen 2 Joint Undertaking under grant agreement no. 779366. This Joint Undertaking receives support from the European Union's Horizon 2020 research and innovation program, Hydrogen Europe and Hydrogen Europe research. The work was supported by the U.K. Engineering and Physical Sciences Research Council under project EP/P024807/1.

Author contributions: A.M. and A.K. conceived the idea and designed the experiments. A.M. and M.G. synthesised the materials and carried out electrochemical tests and physical characterisations. A.K. developed geometrical models of the catalyst. A.M. and M.G. carried out small-size single cell tests. F.J., A.R. and M.-T.S performed Mossbauer measurements and data analysis, A.Z. and A.K. performed XAS measurements, data analysis and fitting, and

interpretation of XANES and EXAFS results, M.P. and P.S. conducted CO chemisorption measurements and data analysis, A.M.B. and D. F. carried out large-size single cell tests, and G.D. performed EDSX-STEM and atomic-resolution STEM measurements and data analysis. A.M., F.J. and A.K. wrote and edited the manuscript with feedback from all the contributing authors. A.K. acted as the project supervisor.

Competing interests: Authors declare no competing interests.

Data and materials availability: All data is available in the main text or the supplementary materials. The data used in the production of the figures in this paper are available for download [DOI inserted after acceptance]